J Math Imaging Vis (2013) 45:214–226
DOI 10.1007/s10851-012-0377-4

Analysis of Scalar Maps for the Segmentation of the Corpus Callosum in Diffusion Tensor Fields

Leticia Rittner · Jennifer S.W. Campbell · Pedro F. Freitas · Simone Appenzeller · G. Bruce Pike · Roberto A. Lotufo

Published online: 13 September 2012

Abstract Diffusion tensor imaging (DTI) is a powerful technique for imaging axonal anatomy in vivo and its automatic segmentation is important for quantitative analysis and visualization. Application of the watershed transform is a recent approach for robustly segmenting diffusion tensor images. Since an important step of the watershed-based segmentation is the gradient computation, this paper investigates scalar maps from DTI and their ability to enhance borders and, therefore, their usefulness in gradient calculation. A comparison between existing scalar maps is conducted in the context of segmentation. New diffusion scalar maps, inspired by mathematical morphology concepts are proposed and included in the comparison. The watershed transform is then applied to segment the corpus callosum, based on the computed scalar maps.

Keywords Diffusion scalar maps · Diffusion tensor imaging · Mathematical morphology · Segmentation · Watershed · Corpus Callosum

L. Rittner (✉) · P.F. Freitas · R.A. Lotufo
School of Electrical and Computer Engineering,
University of Campinas, 13083-852 Campinas, SP, Brazil
e-mail: lrittner@dca.fee.unicamp.br

S. Appenzeller
Department of Rheumatology, University of Campinas,
13083-887 Campinas, SP, Brazil

J.S.W. Campbell · G. Bruce Pike
McConnell Brain Imaging Centre,
Montréal Neurological Institute, McGill University,
H3A 2B4 Montreal, QC, Canada

1 Introduction

Diffusion tensor imaging (DTI) is a relatively new MRI modality capable of generating contrasts that are sensitive to fiber orientations. It carries rich information about intra-white-matter axonal anatomy, which cannot be seen in conventional MRI. DTI-based segmentation, where regions of interest are delineated, is necessary for performing subsequent quantitative analysis and qualitative visualization. While scalar image segmentation has been studied extensively and different algorithms have been developed over the last decades, DTI-based segmentation is a relatively new and challenging task [4].

The use of DTI properties to perform the clustering of brain tissue was initially described by Pierpaoli et al. [32]. More recently, DTI-based clustering strategies have been described [3, 25, 29, 41, 42, 44, 45] and have been applied in many studies, including studies of the thalamic nuclei [11, 17, 18, 43, 45], the thalamocortical projections [7] and the fetal brain [26]. Although the strategies are based on well-known segmentation algorithms, such as level-sets, region growing and graph-cuts, they were actually developed exclusively for DTI. Significant modifications in the original algorithms, conceived to work with scalar images, had to be done in order to deal with tensorial information.

Instead of defining a new segmentation method, the aim of this study is to explore the transformation of diffusion tensor data into scalar maps and the use of these scalar maps, together with the watershed transform, to segment diffusion tensor fields. Preliminary investigation of watershed segmentation of diffusion scalar maps has been done [35], and this paper explores new scalar maps and analyzes the performance of the segmentation with them.

The watershed transform is a region-based segmentation approach and has been successfully applied to the solution of many medical imaging problems, such as the segmentation of blood cells [12], neuromorphometry [13] and characterization of human cortex [9, 33]. It was chosen over other segmentation techniques because it is simple and efficient, and does not require previous knowledge of the structures to be segmented, surface initialization or manual seed placement.

A crucial step of the watershed-based segmentation is the computation of a gradient of the image to be segmented. The magnitude of a gradient can be seen as a scalar map that contains edge information. In the diffusion tensor field context, it is desirable that the gradient helps to find edges between regions with distinct diffusion characteristics. In other words, the gradient should be strong where diffusion changes are significant and weak where diffusion changes are imperceptible.

Several scalar maps based on diffusion measures can be found in the literature, including intra- and intervoxel measures. The mean diffusivity (*MD*), the fractional anisotropy (*FA*) and the volume ratio (*VR*) are examples of intravoxel measures. Other measures, such as the lattice index (*LI*) and the coherence index (*CI*), are classified as intervoxel measures. It is important to point out that none of the above scalar maps were conceived for segmentation purposes and, therefore, they do not necessarily contain enough information to distinguish regions with distinct diffusion characteristics. Recently, we published a technique, called the tensorial morphological gradient (TMG), that was design specifically to be used in the context of segmentation. The TMG transforms the diffusion tensor image into a scalar map with meaningful values to detect borders between brain structures [35]. The tensorial morphological gradient uses diffusion intervoxel measures and combines them to compute a gradient using concepts from mathematical morphology.

The contributions of this work are threefold: first, new scalar maps are proposed by combining mathematical morphology operators and existing measures. Second, we analyze the scalar maps, taking into account their suitability for the segmentation task. Third, segmentation experiments using the watershed transform illustrate the main differences between scalar maps and illuminate which are optimal for segmentation.

This paper is organized as follows: while Sect. 2 presents existing intra- and intervoxel measures, Sect. 3 describes a new class of intervoxel measures being proposed: gradients based on mathematical morphology. The experiments are described in Sect. 4 and results are presented in Sect. 5. Finally, Sect. 6 discusses the obtained results and Sect. 7 concludes the paper.

2 Existing Scalar Measures in Diffusion MRI

2.1 Intravoxel Diffusion Measures

Several properties of the diffusion tensor are rotationally invariant and useful in deriving quantitative information from the diffusion tensor and in comparing different tensors and ellipsoids. The most simple invariant measures obtained from DTI is the mean diffusivity (*MD*), which is one third of the trace of the tensor T:

$$MD = \frac{\text{Trace}(\mathsf{T})}{3} = \frac{\lambda_1 + \lambda_2 + \lambda_3}{3}. \tag{1}$$

Another simple kind of rotationally invariant measure is the "diffusion anisotropy index" or DAI, that gives an idea of the degree of anisotropy of a given diffusion tensor. The common DAIs range from 0 to 1 and do not require eigenvalue sorting. The simplest anisotropy measure is the variance of the three eigenvalues about their mean. The variance alone, however, needs to be normalized to account for regional differences in the overall magnitude of diffusivity. The most used DAI based on this logic is the fractional anisotropy (*FA*) [5] given by:

$$FA = \sqrt{\frac{3}{2}} \frac{\sqrt{(\lambda_1 - MD)^2 + (\lambda_2 - MD)^2 + (\lambda_3 - MD)^2}}{\sqrt{\lambda_1^2 + \lambda_2^2 + \lambda_3^2}}. \tag{2}$$

It normalizes the variance by the magnitude of the tensor as a whole. In other words, *FA* measures the fraction of the tensor that can be assigned to anisotropic diffusion. The *FA* measure is appropriately normalized so that it takes values from zero (isotropic diffusion) to one (anisotropic diffusion).

There are many other ways to represent the anisotropy, such as the scaled relative anisotropy (*sRA*):

$$sRA = \frac{\sqrt{(\lambda_1 - MD)^2 + (\lambda_2 - MD)^2 + (\lambda_3 - MD)^2}}{\sqrt{6}MD}, \tag{3}$$

and the volume fraction (*VF*),

$$VF = 1 - VR = 1 - \frac{\lambda_1 \lambda_2 \lambda_3}{MD^3}, \tag{4}$$

which is obtained by subtracting the volume ratio (*VR*) from unity, in order to scale the measure from 0 to 1 [21].

2.2 Intervoxel Diffusion Measures

The rotationally invariant properties mentioned in the previous section are usually computed for a single voxel and therefore, can be interpreted as an intravoxel measure. Further interesting information can be obtained by looking at how the tensor parameters estimated in a given voxel compare with those in neighboring voxels. The simplest way to

do this is to use measures that quantify the distance (or the difference) between two neighboring tensors. Another approach is to compute the differences (or coherences) within a neighborhood of a tensor and combine all the obtained quantities into a single measure, that can be interpreted as a homogeneity (or inhomogeneity) measure.

2.2.1 Diffusion Tensor Distances

Distance between tensors can also be viewed as intervoxel measures. Given two tensors T_i and T_j, the most simple comparison between two tensor quantities, used by Ziyan et al. [45], is the dot product (*DP*) between the principal eigenvector directions:

$$d_1(\mathsf{T}_i, \mathsf{T}_j) = |e_{1,i} \cdot e_{1,j}|, \tag{5}$$

where $e_{1,i}$ and $e_{1,j}$ are the principal eigenvectors of tensors T_i and T_j, respectively. Another simple similarity measure, presented by Pierpaoli et al. [32] as an intervoxel anisotropy measure, is the tensor dot product (*TDP*):

$$d_2(\mathsf{T}_i, \mathsf{T}_j) = \mathsf{T}_i : \mathsf{T}_j = \sum_{k=1}^{3}\sum_{l=1}^{3}(\sqrt{\lambda_{k,i}}\sqrt{\lambda_{l,j}}e_{k,i} \cdot e_{l,j})^2. \tag{6}$$

Alexander et al. [1] proposed a number of tensor similarity measures. Their purpose was to match pairs of diffusion tensor images and the proposed measures were based on the diffusion tensor itself and indices derived from the diffusion tensor. One of the similarity measures proposed by them was obtained by negating the following Euclidean distance metric:

$$d_3(\mathsf{T}_i, \mathsf{T}_j) = \sqrt{\mathrm{Trace}\big((\mathsf{T}_i - \mathsf{T}_j)^2\big)}. \tag{7}$$

This similarity metric was also explored in other DTI studies under different names, such as generalized tensor dot product and Frobenius norm [19, 43, 45]. As affine invariance is a desirable property for segmentation purposes and the Frobenius norm (*FN*) is not invariant to affine transformations, Wang and Vemuri [41] proposed a novel definition of diffusion tensor "distance", as the square root of the J-divergence (*Jdiv*) of the corresponding Gaussian distributions, i.e.,

$$d_4(\mathsf{T}_i, \mathsf{T}_j) = \frac{1}{2}\sqrt{\mathrm{Trace}\big(\mathsf{T}_i^{-1}\mathsf{T}_j - \mathsf{T}_j^{-1}\mathsf{T}_i\big) - 2n}, \tag{8}$$

where n is the matrix size that represents the tensor. Equation 8 is not a true distance since it violates the triangle inequality, but it is in fact a computationally efficient approximation of Rao's distance [41]. More recently, a new approach for calculating tensor similarity has been adopted in DTI studies: the Log-Euclidean distances. Among the similarity metrics proposed by Arsigny et al. [2], there is a metric very closely related to the Frobenius norm, called the similarity-invariant Log-Euclidean distance (*LogE*), defined as :

$$d_5(\mathsf{T}_i, \mathsf{T}_j) = \sqrt{\mathrm{Trace}\Big(\big(\log(\mathsf{T}_i) - \log(\mathsf{T}_j)\big)^2\Big)}. \tag{9}$$

Contrary to the classical Euclidean framework on tensors, one can see from Eq. 9 that symmetric matrices with null or negative eigenvalues are at an infinite distance from any tensor. To overcome this problem, in this paper we replace $\log(\mathsf{T}_i)$ by $\log(100 * \mathsf{T}_i + 1)$ to avoid the computation of the logarithm of null values.

Another affine invariant metric for statistical analysis and image processing of diffusion tensor data based on the Riemannian geometry was introduced independently by different authors [6, 31]:

$$d_6(\mathsf{T}_i, \mathsf{T}_j) = \sqrt{\mathrm{Trace}\big(\log(\mathsf{D}_{ij})^2\big)}, \tag{10}$$

where D_{ij} is equal to $\mathsf{T}_i^{-\frac{1}{2}}\mathsf{T}_j\mathsf{T}_i^{-\frac{1}{2}}$.

It is important to notice that the mentioned intervoxel distance measures are not the only ones proposed in the literature. They were chosen to be part of this study because they come from different approaches and privilege specific aspects of the tensor. Peeters et al. [30] presented a classification of the intervoxel distance measures based on their derivation: measures based on scalar indices; measures that make use of the angles between eigenvectors; measures based on linear algebra; measures based on Riemannian geometry; measures considering the tensors as a representation of a probability density function and measures that combine different measures from the previous classes. Hence, whereas the dot product is an angular difference, the tensor dot product and the Frobenius norm come from linear algebra, the Log-Euclidean distance and the affine-invariant Riemannian metric (Riem) are based on Riemannian geometry and the J-divergence derives from statistical considerations.

2.2.2 Neighborhood Anisotropy Measures

Intervoxel anisotropy measures were introduced by Pierpaoli and Basser [32] and extended by Skare et al. [38] to reduce the effect of noise. The principle is to perform spatial averaging of indices based on both eigenvalues and eigenvectors.

One example of such a diffusion anisotropy measure is the A_{dd}, that measures how much the directions of the tensor eigenvectors differ between a given voxel and its neighbors, and is defined as:

$$A_{dd} = \frac{\sum_1^8 a_N A_{dd}^N}{\sum a_N}, \tag{11}$$

where

$$A_{dd}^N = \frac{\hat{\mathsf{T}}_i : \hat{\mathsf{T}}_j}{\mathsf{T}_i : \mathsf{T}_j} \tag{12}$$

and the tensor dot product between the anisotropic parts of the tensor $\hat{\mathsf{T}}_i : \hat{\mathsf{T}}_j$ is given by:

$$\hat{\mathsf{T}}_i : \hat{\mathsf{T}}_j = \mathsf{T}_i : \mathsf{T}_j - \frac{1}{3}\text{Trace}(\mathsf{T}_i)\text{Trace}(\mathsf{T}_j). \tag{13}$$

Another measure, first described by Klingberg et al. [23], is the coherence index (*CI*). The *CI* in a voxel is the mean dot-product of the primary eigenvector of the reference voxel and the primary eigenvector of each one of its eight neighboring voxels. When the eigenvectors are of unit length, the dot product is the cosine of the angle between the primary eigenvectors of both tensors and has a value between 0 and 1.

2.2.3 Tensorial Morphological Gradient (TMG)

The tensorial morphological gradient (TMG) is an intervoxel diffusion measure based on mathematical morphology. It was first applied to segment tensorial images representing color images [36, 37] and its concept was then extended and applied to synthetic diffusion tensor images [34]. It is based on mathematical morphology and intervoxel distances between neighboring tensors.

While the classical morphological gradient at each point of a scalar image yields the difference between the maximum and the minimum values over the neighborhood at the point determined by a structuring element, the tensorial morphological gradient (TMG) [36] of a tensorial image is defined by:

$$\nabla_B^{\mathsf{T}}(f)(x) = \bigvee_{y,z\in B_x} d_n(\mathsf{T}_y, \mathsf{T}_z), \tag{14}$$

$\forall x \in E$, where d_n represents any of the intervoxel distances presented in Sect. 2.2.1, $B \subset E$ is a structuring element centered at the origin of E, T_y is the tensor that represents the diffusion in y, and T_z is the tensor that represents the diffusion in z (y and z are in the neighborhood of x, defined by B_x). ∇_B^{T} is the proposed TMG. Because the intervoxel measures are already comparisons between neighbors, the proposed gradient is not the difference between the maximum and the minimum values, but only the maximum value.

3 Gradients: A New Intervoxel Diffusion Measures Class

In previous works, a tensorial morphological gradient (TMG) was conceived to allow the segmentation of diffusion tensor fields by the watershed transform. Experiments depicted that the TMG is able to preserve borders while transforming the diffusion tensor filed in a scalar map, a desirable requisite of gradients to be used in segmentation tasks. Inspired by the good results obtained by the tensorial morphological gradient, a new class of intervoxel diffusion measures is being proposed: gradients based on mathematical morphology. This new class of diffusion measures are, therefore, composed by the tensorial morphological gradient (TMG) of diffusion intervoxel measures and the morphological gradient (MG) of diffusion intravoxel measures.

The morphological gradient (MG) is the most common gradient based on mathematical morphology used in image processing [16], and depends on the size and shape of the chosen structuring element. Let E be the set of all points in the image. Using a flat structuring element at each point, the morphological gradient (MG) yields the difference between the maximum and the minimum values over the neighborhood at the point determined by the flat structuring element:

$$\nabla_B^I(f) = \bigvee_{y\in B_x} \mathbf{I}_y - \bigwedge_{y\in B_x} \mathbf{I}_y, \tag{15}$$

where $B \subset E$ is a structured element centered at the origin of E and $\mathbf{I}_y$ is the intensity value in y (y is in the neighborhood of x, defined by B_x).

Because the diffusion tensor image does not have a single intensity value to be considered in the morphological gradient computation, the proposed solution is to compute the morphological gradient of any intravoxel measure presented in Sect. 2.1, obtaining a new class of intervoxel measures. As an example, by taking the fractional anisotropy FA_y as the $\mathbf{I}_y$, it is possible to compute the morphological gradient of the fractional anisotropy (MG-*FA*):

$$\nabla_B^{FA}(f) = \bigvee_{y\in B_x} FA_y - \bigwedge_{y\in B_x} FA_y. \tag{16}$$

Although the *FA* is an intravoxel measure, by computing its morphological gradient, information of the neighborhood is incorporated, resulting in an intervoxel measure. As with the TMG, the neighborhood intervoxel measures presented in Sect. 2.2.2 (A_{dd} and *CI*) result from comparison between tensors in the neighborhood using intervoxel measures. The main difference between them and the TMG is that the TMG takes the maximum between the computed intervoxel measurements while the A_{dd} and the *CI* take the average of the measurements (weighted or not by the distance of each neighbor).

Hence, it is possible to extend the definition of the TMG to A_{dd} (TMG-A_{dd}), for example, defining a new measure:

$$\nabla_B^{A_{dd}}(f)(x) = \bigvee_{y,z\in B_x} A_{dd}(\mathsf{T}_y, \mathsf{T}_z). \tag{17}$$

By using the same reasoning, it is easy to conclude that the extension of the Coherence Index (*CI*), originally computed as the mean value of the dot product within a defined neighborhood, is the TMG based on the dot product (TMG-*DP*). Furthermore, whereas the neighborhood in the *CI* computation is fixed as a square around the voxel (8 neighbors), the neighborhood in the TMG-*DP* computation is defined by the structuring element and can be chosen accordingly to the application.

Table 1 Summary of existing intra and intervoxel measures, their rotationally invariance and their dependence on eigenvalues and eigenvectors

	Measure	Rot. Inv.	Eigenval.	Eigenvec.
Intravoxel	*MD*	yes	yes	no
	FA	yes	yes	no
	VF	yes	yes	no
	sRA	yes	yes	no
Intervoxel	*DP*	yes	no	yes
	TDP	yes	yes	yes
	FN	no	yes	yes
	Jdiv	yes	yes	yes
	Riem	yes	yes	yes
	LogE	no	yes	yes
	A_{dd}^N	yes	yes	yes

Table 2 Summary of proposed neighborhood measures, concerning their computation method: mean, maximum or difference between the maximum and the minimum value within the neighborhood

Original measure		Operator	Neighborhood measure[a]
Intravoxel	*MD*	max − min	MG-*MD*
	FA	max − min	MG-*FA*
	VF	max − min	MG-*VF*
	sRA	max − min	MG-*sRA*
Intervoxel	*DP*	mean	*CI*
		max	TMG-*DP*
	TDP	max	TMG-*TDP*
	FN	max	TMG-*FN*
	Jdiv	max	TMG-*Jdiv*
	Riem	max	TMG-*Riem*
	LogE	max	TMG-*LogE*
	A_{dd}^N	mean	A_{dd}
		max	TMG-A_{dd}

[a]Proposed by the authors, except *CI* and A_{dd}

Tables 1 and 2 summarize all intravoxel and intervoxel measures presented in Sects. 2 and 3. Table 1 lists the existing voxelwise measures and points out whether the intravoxel and intervoxel measures are rotationally invariant or not, based on the eigenvalues and/or eigenvectors. Table 2 lists each neighborhood measure and identifies which measure it is based on, and whether it is an average of the measure within a neighborhood (mean), the biggest difference between neighbors (max − min) or it is the maximum measure found in the neighborhood (max). It is valuable to note that the measures listed in the last column of Table 2, with the exception of *CI* and A_{dd}, are the ones based on mathematical morphology and proposed by the authors.

4 Methods

4.1 Acquisition of Human Brain Data

Real data were acquired on a Siemens 3T Trio MR scanner with $N = 30$ diffusion encoding directions, 63 slices, 2.0 mm × 2.0 mm × 2.0 mm, TE = 95 ms, TR = 8.7 s and $b = 1000$ s/mm^2. Fifteen human subjects were scanned. The diffusion data was first linearly interpolated before tensor estimation and the negative eigenvalues were replaced with zero [24]. The MINC tools[1] from the Montreal Neurological Institute, McGill University, were used for all diffusion image preprocessing.

4.2 Segmentation Experiments

In order to compare the performance of distinct diffusion scalar measures when used together with the watershed in DTI-based segmentation of white matter structures we studied the corpus callosum. The corpus callosum is the major white matter structure and conduit for information transfer between the cerebral hemispheres and plays an integral role in relaying sensory, motor and cognitive information between homologous cortical regions.

The original image was cropped around the corpus callosum to a subvolume of size 33 × 44 × 21 voxels (xyz orientation). Although the scalar maps would not differ if calculated for the entire image (brain) or only for a cropped version of it, the watershed results would suffer considerably if run for the entire brain. In order to detect all the borders of the corpus callosum, the number of regions chosen for the hierarchical watershed would have to be increased tremendously, since several markers would appear outside the corpus callosum. In other words, the method would attempt to detect all borders inside the brain, even the ones not related to the corpus callosum, and would have less precision in the corpus callosum region. In the other hand, when the image is cropped around the corpus callosum, the watershed transform concentrates its efforts on distinguishing the corpus callosum from the background.

Intravoxel and intervoxel maps were computed and visualized. All morphological gradients were computed using a 3 × 3 diamond structuring element and the measures based on the average used the 8-connected two-dimensional neighborhood of the reference tensor. The 8-connected neighborhood was used because of the original definition of *CI* and A_{dd}, even though a 6-connected three-dimensional neighborhood is expected to result in a better scalar map.

The diffusion scalar maps were analyzed in the context of the segmentation task. After computation of the scalar

[1] http://www.bic.mni.mcgill.ca/ServicesSoftware/MINC.

maps, the hierarchical segmentation was achieved by the application of the 3D watershed from markers [8, 10, 14, 40] and extinction values computation [15, 27, 28, 39]. In other words, after calculating the scalar map of the original image, the n structures in the image which had the greatest volume extinction values were automatically selected. The n markers assigned to these regions were then used in the watershed transform, which segmented the scalar map into n regions.

The main goal of the segmentation experiments was to identify which scalar maps were able to successfully segment the corpus callosum for all fifteen sets of real data. A segmentation was considered successful if it was able to segment the corpus callosum as only one connected component.

The results obtained by the watershed using the scalar measures able to segment the corpus callosum successfully for all datasets, i.e., the MG-*FA*, A_{dd} and the TMG-A_{dd}(max), were compared to manual segmentation results, in order to evaluate the performance of the segmentation. Since there was no segmentation ground truth for comparison, the definition of a segmentation standard was based on manual segmentations made by specialists, as described by Kaus et al. [20]. Three specialists delineated the corpus callosum boundaries in the *FA* map and the standard segmentation in each subject image was defined as those voxels labeled as corpus callosum by at least two specialists. All other voxels were labeled as background.

Two different metrics were used to evaluate the obtained segmentation in comparison with the standard: kappa and overlap [22]. The kappa coefficient measures the agreement of the segmentations, taking into account the probability of random agreement. The overlap metric is defined as the percentage of voxels classified as corpus callosum by both the method and the standard with respect to the number of voxels classified as corpus callosum by at least one of them.

Other metrics, such as accuracy and specificity, were not used to compare the obtained segmentations because their values take into account the voxels labeled as background by both the method and the standard. As the background area is significantly larger than the corpus callosum, high values do not necessarily reflect good performance of the proposed method.

5 Results

5.1 Segmentation Experiments

An example of a real diffusion tensor image is presented in Fig. 1. The original image is a DT image of the brain. The eigenvalues from the DTI (λ_1, λ_2 and λ_3) are shown in Figs. 1(a)–(c), the principal eigenvector direction (PED) (color-coded map) in Fig. 1(d) and the manual segmentation in Fig. 1(e).

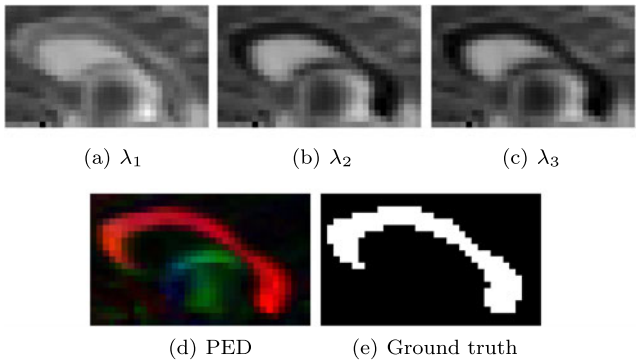

Fig. 1 DTI of the corpus callosum—each eigenvalue (λ_1, λ_2 and λ_3) shown separately, the principal eigenvector direction (PED) and the result of manual segmentation. Small λ_2 and λ_3 and uniform color of the PED confirm that the corpus callosum is a highly oriented structure

Although the original image is volumetric ($33 \times 44 \times 21$ voxels), only one slice is presented, in order to facilitate visualization. All scalar measures cited in Sect. 2 were computed for the original DT image and presented in Figs. 2, 3, and 4. Intravoxel measures can be seen in Figs. 2(a)–(d), intervoxel measures based on the morphological gradient (max − min) of intravoxel measures are presented in Figs. 2(e)–(h) and their respective segmentation by the hierarchical watershed in Figs. 2(i)–(l). Figures 3(a)–(e) and 3(k)–(l) show the tensorial morphological gradients based on intervoxel measures (*Jdiv*, *TDP*, *FN*, *Riem*, *LogE*, *DP* and A^N_{dd}) and Figs. 3(f)–(j) and 3(m)–(n) present their respective watershed-based segmentation. Finally, Figs. 4(a)–(b) present neighborhood anisotropy measures based on average, *CI* and A_{dd}, and Figs. 4(c)–(d) their respective watershed-based segmentation.

In the example shown in Fig. 2, it is possible to confirm that transitions between regions of low and high anisotropy are smooth in the *FA* map (Fig. 2(b)) and more abrupt in the *VF* map (Fig. 2(c)), due to its lack of sensitivity in less anisotropic regions. The corpus callosum, therefore, seems bigger in the *FA* map than in the VF map and different segmentations result (Figs. 2(j) and 2(k)). On the other hand, although the MG-*FA* from Fig. 2(f) is much more noisy outside the corpus callosum than the MG-*VF* from Fig. 2(g), the segmentation result did not suffer distortions due to this noise and looks more similar to the ground truth (Fig. 1(e)).

By using the same intervoxel measures from Sect. 2 in the TMG computation, it is possible to verify the adequacy of a scalar map to detect borders of the corpus callosum. The *DP* and the *TDP*, unable to detect differences between distinct tensors with the same orientation, were able to preserve important borders in the corpus callosum experiment, as shown in Figs. 3(k) and 3(b). The *FN*, which is not affine invariant, also provided a useful scalar map (Fig. 3(c)), when used to compute the TMG.

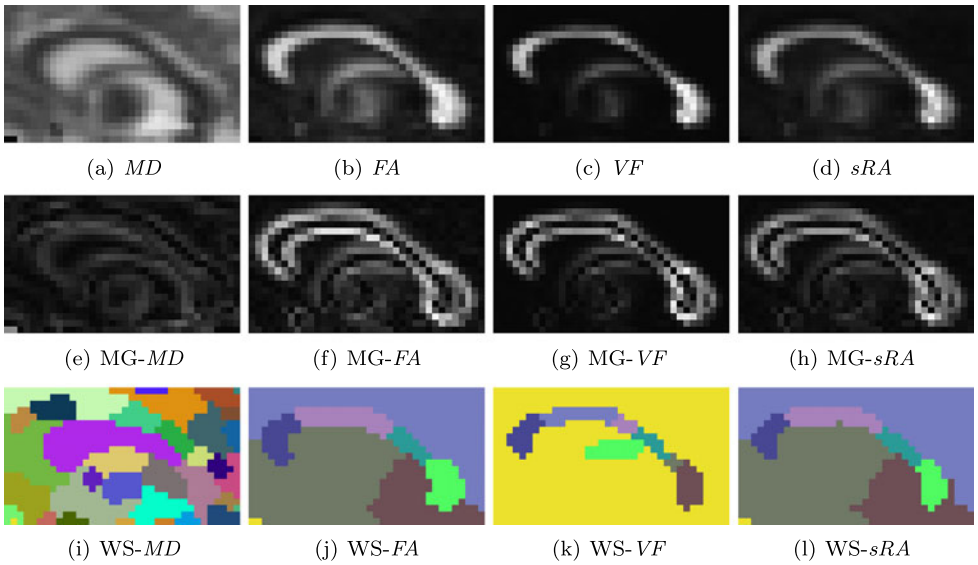

Fig. 2 Intravoxel measures—*MD*, *FA*, *VF* and *sRA*, respective morphological gradient (MG) and resulting watershed segmentation. The MGs were computed using a 6-connected neighborhood as structuring element

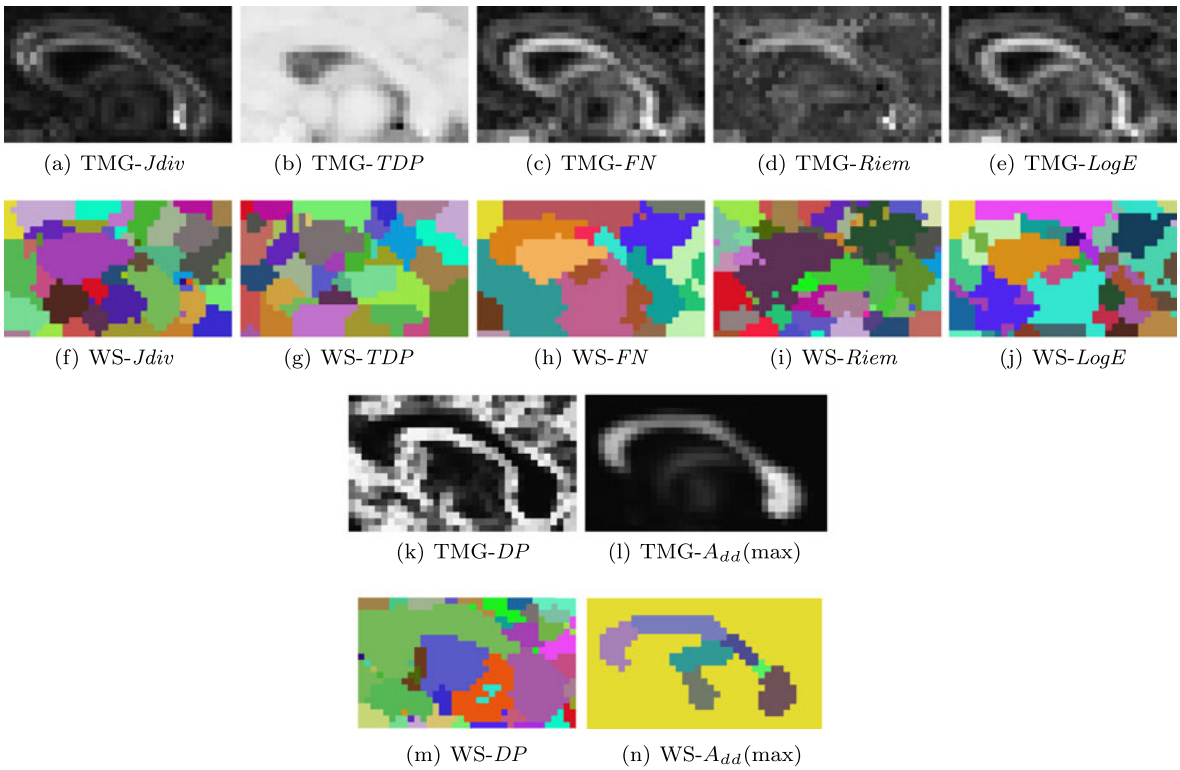

Fig. 3 TMGs computed using each intervoxel measure presented in Sect. 2.2.1 and the respective obtained watershed-based segmentation

The gradients based on *Jdiv* (Fig. 3(a)), on *TDP* (Fig. 3(b)) and on *Riem* (Fig. 3(d)) presented smoother borders, and consequently the segmentation result provided by them are inferior (Figs. 3(f), 3(g) and 3(i)). The borders in the TMG using *FN* (Fig. 3(c)), *LogE* (Fig. 3(e)) and A_{dd} (Fig. 3(l)) were sharper and provide better results in the application of the watershed technique. Although the TMG using *DP* (Fig. 3(k)) presents strong borders, its obtained segmentation was not good due to the discontinuity in its upper border.

The neighborhood intervoxel measures presented in Figs. 4(a) and 4(b) seem able to preserve the borders of corpus callosum, especially the A_{dd}. However, its counterpart, presented in Figs. 3(k) and 3(l), accomplish the segmentation task with superiority when compared to the ground truth, thanks not only to the replacement of the mean by the

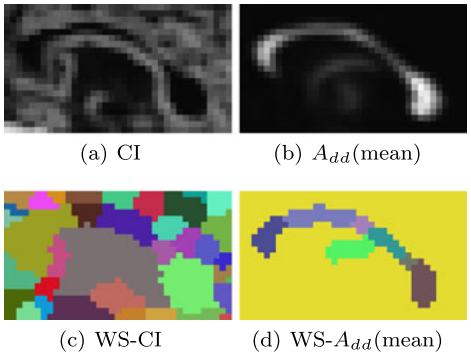

(a) CI (b) A_{dd}(mean)

(c) WS-CI (d) WS-A_{dd}(mean)

Fig. 4 Neighborhood anisotropy measures computed for the corpus callosum region

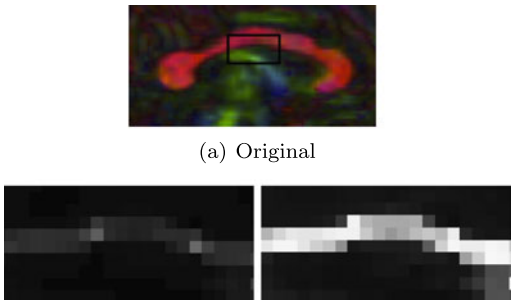

(a) Original

(b) CI (c) CI-TMG

Fig. 5 Comparison of the coherence index (*CI*) and the *CI*-TMG computed using the dot product as similarity measure. Both were obtained using a 6-connected three-dimensional neighborhood and are showed only in the detail marked by the *rectangle* in the original image

maximum (see Eqs. 11 and 17, for example), but also due to the neighborhood being considered in their computation.

Figure 5(a) shows the principal eigenvector direction (PED) of the corpus callosum, with a detail selected on it. A better solution to help the scalar map *CI* to preserve borders would be to use a 3D neighborhood in its computation. But even when a 3D neighborhood (6-connected neighbors) is considered instead of a 2D neighborhood (8-connected neighbors), the *CI* result (Fig. 5(b)) is considerably inferior, when compared to the TMG (Fig. 5(c)). Similar conclusions can be drawn about A_{dd}, since the neighbors used in its computation are, by definition, also from a single plane.

Not all scalar maps presented similar segmentation performance for all 15 subjects. For some subjects, the TMGs were able to segment the corpus callosum as a single connected component (Figs. 6(a) and 6(b)), even for a small number of regions ($n = 25$). For other subjects, in which the corpus callosum presented a thinner profile, the TMGs were not able to distinguish it from the background (Figs. 6(c) and Fig. 6(d)), even for a large number of regions ($n = 100$). Some morphological gradients, MG-*sRA* and MG-*VF*, were not able to segment only one connected component representing the corpus callosum for some subjects, no matter the

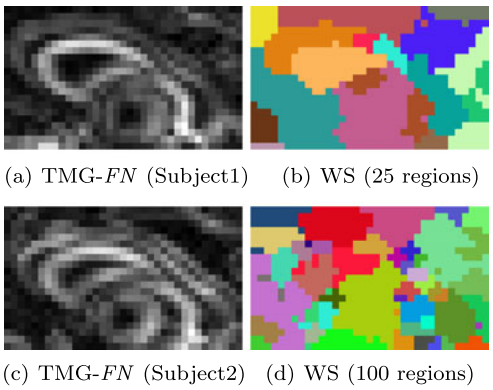

(a) TMG-*FN* (Subject1) (b) WS (25 regions)

(c) TMG-*FN* (Subject2) (d) WS (100 regions)

Fig. 6 Watershed segmentation results based on the TMG-*FN* for two subjects. For the first subject, where the watershed was able to segment the corpus callosum, the chosen number of regions n was 25. For the second subject, even with $n = 100$, the watershed was not able to segment the corpus callosum

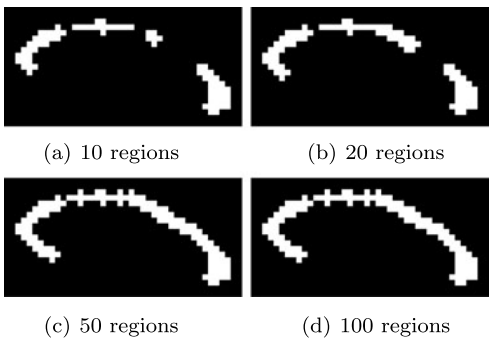

(a) 10 regions (b) 20 regions

(c) 50 regions (d) 100 regions

Fig. 7 Segmentation using MG-*VF* computed for the corpus callosum region, varying the number of regions (10, 20, 50 and 100)

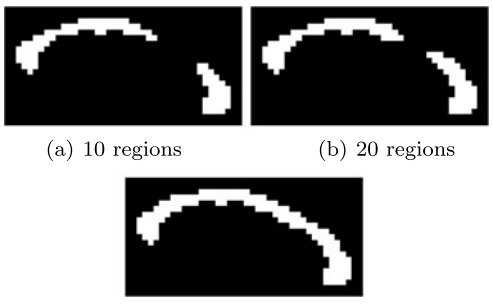

(a) 10 regions (b) 20 regions

(c) 50 regions

Fig. 8 Segmentation using MG-*FA* computed for the corpus callosum region, varying the number of regions (10, 20 and 50)

value assigned for n (Fig. 7). Other scalar maps, such as the MG-*FA*, the A_{dd} and the TMG-A_{dd}(max), were able to segment all datasets, depending only on a good choice of the number n of regions (Fig. 8).

The summary of segmentation results can be seen in Fig. 9. While the MG-*FA*, A_{dd} e TMG-A_{dd}(max) were able to segment all 15 subjects, the MG-*sRA* and the MG-*VF* succeeded for 14 subject and failed to segment the corpus cal-

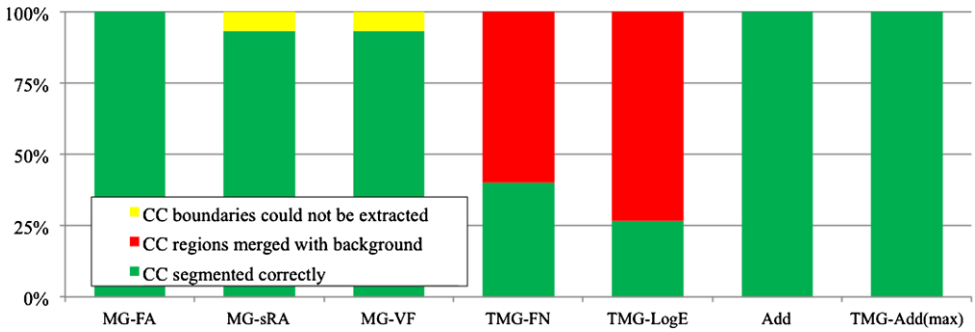

Fig. 9 Number of successful and unsuccessful segmentations within the dataset using several scalar measures: correctly segmented (*green*); the corpus callosum as 2 connected components (*yellow*) and missing borders of the corpus callosum (*red*) (Color figure online)

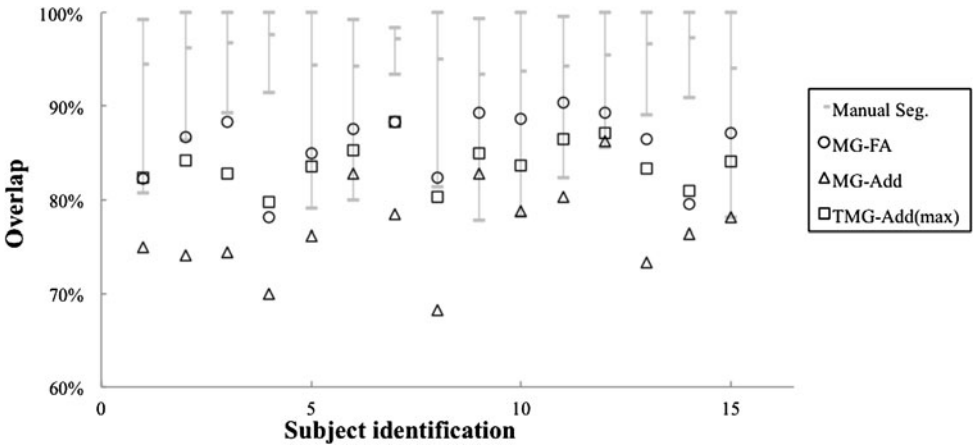

Fig. 10 Overlap of manual and automatic segmentation results compared to the gold standard for all 15 subjects

losum as one connected component for only 1 subject. The TMG-*FN* and the TMG-*LogE* failed to detect all the corpus callosum borders for 9 and 11 subjects, respectively.

The scalar maps which were able to segment the corpus callosum as one connected component for all fifteen sets of real data had their segmentation results quantitatively assessed. The minimum, maximum and mean overlap of the manual segmentation versus the standard were computed separately for each subject (Fig. 10). Also the overlap of the watershed segmentation using all three measures in each subject were calculated and plotted (Fig. 10).

The segmentation obtained using the morphological gradient of *FA* (MG-*FA*) presented higher overlap and kappa coefficients, when compared to the other two measures, A_{dd} and TMG-A_{dd}(max). And although it was inferior to the overlap and kappa coefficients of the mean of the manual segmentation, it presented lower variation. The TMG-A_{dd}(max) segmentation performed better then the A_{dd}, when compared to the standard (Table 3).

The volumetric segmentation of the corpus callosum can also be visualized and compared to the manual segmentation. The segmentation result shown in Fig. 11 (red) was obtained using the MG-*FA*, which has shown the best quantitative results, and overlaid to the manual segmentation done by a specialist (green). Most of the voxels assigned as corpus callosum by the specialist are also identified as corpus callosum using the proposed method. As the volumetric boundaries of the corpus callosum are not well defined, as they are in the midsagittal slice, the watershed segmentation can go beyond the specialist segmentation because it is difficult, even for a specialist, to tell exactly where the corpus callosum ends.

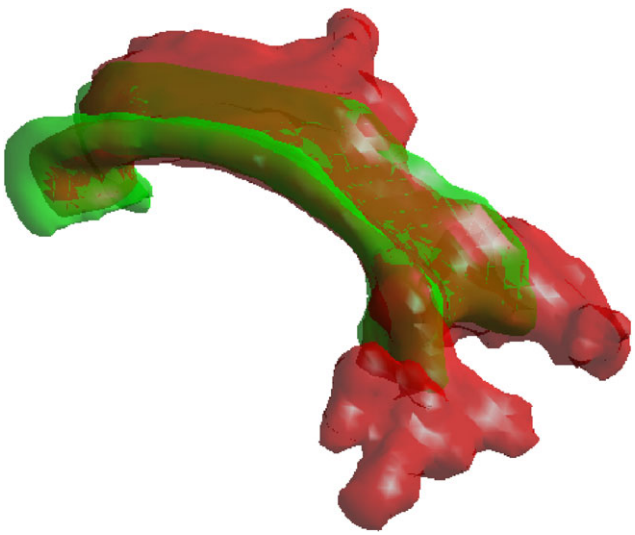

Fig. 11 Automatic (*red*) segmentation result obtained by the watershed transform and the MG-*FA* overlaid on manual (*green*) segmentation (Color figure online)

Table 3 Mean overlap and kappa metrics with their respective standard deviations, computed for segmentation results of all subjects (manual segmentation, watershed segmentation using MG-*FA*, A_{dd} and TMG-A_{dd}(max))

	Overlap		Kappa		Accuracy	
	Mean	Std	Mean	Std	Mean	Std
MG-*FA*	85.96	3.73	92.29	2.22	99.74	0.06
A_{dd}	76.98	4.85	86.76	3.12	99.59	0.10
TMG-A_{dd}(max)	83.79	2.45	91.02	1.46	99.69	0.05
Manual	93.86	7.61	96.60	4.30	99.89	0.13

6 Discussion

DTI is an important MRI technique that allows the investigation and characterization of brain connectivity, and some DTI-based segmentation methods have been studied in the last decade, mostly analyzing white matter structures, due to its high anisotropy [3, 25, 29].

In previous work, a DTI-based segmentation method using the watershed transform and a tensorial morphological gradient was proposed and applied to segment brain structures [35]. Since a crucial step in the proposed method is the computation of the gradient, the present study analyzes the existing diffusion scalar maps as gradient candidates for the watershed method.

Several diffusion scalar maps have been proposed and used mostly in clinical studies, to infer microstructural characteristics of normal tissue and pathological changes in tissue microstructure [5]. This work is the first time that several diffusion scalar maps are analyzed in the context of watershed segmentation.

The visualization of intervoxel maps of the corpus callosum showed that, although it has a mean diffusivity and an anisotropy very similar to its neighbor (the cingulum bundle), all morphological gradients (MGs) computed based on the intervoxel DAIs preserved the borders. The watershed transform based on any of the computed morphological gradients, except the MG-*MD*, was able to segment the corpus callosum. It is separable because of a strip of artifactually low anisotropy between it and the cingulum bundle, due to partial volume averaging of fibres from these two pathways.

Since the diffusion tensors in the corpus callosum are strongly oriented and their orientation differs considerably from that of their neighbors, measures that take into account tensor orientation also performed well in detecting its borders.

Segmentation experiments using the watershed transform showed that the segmentation of the corpus callosum is possible using almost all discussed scalar maps. Nevertheless, when dealing with the variety of shapes and sizes contained within the dataset, only a few measures are able to recover the borders of the corpus callosum.

The scalar maps can be divided in three groups, in terms of the segmentation results obtained. The first group is composed by measures that are not able to segment successfully any data: MG-*MD*, TMG-*DP*, TMG-*TDP* and TMG-*Riem*. The second group is composed by measures that are not able to segment the whole dataset, but only a subset of it. These measures are the morphological gradients, MG-*sRA* and MG-*VF* and both tensorial morphological gradients, TMG-*FN* and TMG-*LogE*. They fail in segmenting thin profiles, where voxels from the corpus callosum and from the background are used simultaneously in the TMG computation of a single voxel. In such cases, these metrics would obtain a better segmentation if computed in interpolated images.

Comparing the TMGs with the DAIs and with the MGs, it is evident that the TMGs are richer in detail, since they take into account much more information. The DAIs are the most simple measures, taking into account only the eigenvalues of each voxel. The MGs are an intervoxel version of the intravoxel DAIs.

Despite being simpler, the MGs were the only ones to segment correctly the entire dataset. The neighborhood is also included in the computation of the tensorial morphological gradients (TMGs), but while the MGs are based on intravoxel measures (i.e., consider only the eigenvalues), the TMGs are based on intervoxel measures, and therefore include information from the eigenvectors in addition to the eigenvalues. Because the eigenvalues carry the most relevant difference between the corpus callosum and the background, measures that take into account the eigenvectors only dilute the important information and result in gradients with weaker borders.

Even though the best segmentation results were obtained by using the MGs, segmentation resulting from the watershed combined with the MG-*sRA* and the MG-*VF* were not satisfactory. Such scalar maps tend to make thin white matter structures even thinner, thanks to their decreased sensitivity in the high anisotropy range. Therefore, even using the external morphological gradient and a high number of regions n, the corpus callosum was not obtained as one single connected component for all subjects.

The comparison of the segmentation results obtained from the watershed with the gold standard constructed from the manual segmentation showed that the MG-*FA* was able to segment two thirds of the dataset as well as the specialists. When looking at the volumetric segmentation results, the MG-*FA* was also the scalar map that performed best. But since the majority of the voxels considered as corpus callosum by the specialist do not present a significant change in the direction of the fibers, the result could be enhanced if the fractional anisotropy map were weighted by the component of the main eigenvector in the most common direction observed. The choice of markers to represent specifically the corpus callosum and the background, not the local minima of the image, could help to reduce the leak of the watershed regions and to perform the segmentation automatically.

7 Conclusions

In this work, tensor-derived maps, usually used in quantitative analysis of DTI, were studied in the context of segmentation. Existing intravoxel and intervoxel maps were discussed, and new scalar maps were proposed, based on concepts of mathematical morphology. All scalar maps were used together with the watershed transform to segment the corpus callosum. The MG-*FA*, the A_{dd} and TMG-A_{dd}(max) preserve relevant information from diffusion tensor images useful for the segmentation task, and therefore are able to segment successfully the corpus callosum for all 15 subjects of the dataset. Other studied scalar maps, such the tensorial morphological gradients TMG-*FN* and TMG-*LogE* and the morphological gradients MG-*VF* and MG-*sRA*), have some difficulty to detect thin structures and, therefore, segmented the corpus callosum as a single connected component only for some subjects. The remaining scalar maps were not able to successfully segment the corpus callosum for any subject.

Acknowledgements The authors would like to thank the National Council for Scientific and Technological Development (CNPq), the Federal Agency of Support and Evaluation of Postgraduate Education (CAPES), the São Paulo Research Foundation (FAPESP) and Natural Sciences and Engineering Research Council of Canada (NSERC) for funding.

References

1. Alexander, D., Gee, J., Bajcsy, R.: Similarity measures for matching diffusion tensor images. In: Brit. Mach. Vision Conf, vol. 1, pp. 93–102 (1999)
2. Arsigny, V., Fillard, P., Pennec, X., Ayache, N.: Log-Euclidean metrics for fast and simple calculus on diffusion tensors. Magn. Reson. Med. **56**(2), 411–421 (2006)
3. Awate, S., Gee, J.: A fuzzy, nonparametric segmentation framework for DTI and MRI analysis. In: Information Processing in Medical Imaging, vol. 20, pp. 296–307 (2007)
4. Barbieri, S., Bauer, M.H., Klein, J., Moltz, J., Nimsky, C., Hahn, H.K.: DTI segmentation via the combined analysis of connectivity maps and tensor distances. NeuroImage **60**(2), 1025–1035 (2012)
5. Basser, P., Pierpaoli, C.: Microstructural and physiological features of tissues elucidated by quantitative-diffusion-tensor MRI. J. Magn. Reson. **111**(3), 209–219 (1996)
6. Batchelor, P.G., Moakher, M., Atkinson, D., Calamante, F., Connelly, A.: A rigorous framework for diffusion tensor calculus. Magn. Reson. Med. **53**(1), 221–225 (2005)
7. Behrens, T.E., Johansen-Berg, H., Woolrich, M.W., Smith, S.M., Wheeler-Kingshott, C.A., Boulby, P.A., Barker, G.J., Sillery, E.L., Sheehan, K., Ciccarelli, O., Thompson, A.J., Brady, J.M., Matthews, P.M.: Non-invasive mapping of connections between human thalamus and cortex using diffusion imaging. Nat. Neurosci. **6**(7), 750–757 (2003)
8. Beucher, S., Meyer, F.: The morphological approach to segmentation: the watershed transformation. In: Dougherty, E.R. (ed.) Mathematical Morphology in Image Processing, pp. 433–481. CRC Press, Boca Raton (1992)
9. Castellano, G., Lotufo, R., Falcão, A., Cendes, F.: Characterization of the human cortex in MR images through the image foresting transform. In: International Conference on Image Processing, vol. 1, pp. 357–360 (2003)
10. Cousty, J., Bertrand, G., Najman, L., Couprie, M.: Watershed cuts: minimum spanning forests and the drop of water principle. IEEE Trans. Pattern Anal. Mach. Intell. **31**(8), 1362–1374 (2009)
11. Duan, Y., Li, X., Xi, Y.: Thalamus segmentation from diffusion tensor magnetic resonance imaging. Int. J. Biomed. Imaging **2007**, 1–5 (2007)
12. Falcão, A., Cunha, B., Lotufo, R.: Design of connected operators using the image foresting transform. In: SPIE on Medical Imaging, vol. 4322, pp. 468–479 (2001)
13. Falcão, A., Costa, L., da Cunha, B.: Multiscale skeletons by image foresting transform and its applications to neuromorphometry. Pattern Recognit. **35**(7), 1571–1582 (2002)
14. Falcão, A., Stolfi, J., Lotufo, R.: The image foresting transform: theory, algorithms, and applications. IEEE Trans. Pattern Anal. Mach. Intell. **26**(1), 19–29 (2004)
15. Grimaud, M.: A new measure of contrast: the dynamics. In: Image Algebra and Morphological Image Processing III, vol. 1769, pp. 292–305 (1992)
16. Heijmans, H.J.A.M.: Morphological Image Operators. Academic Press, Boston (1994)
17. Johansen-Berg, H., Behrens, T., Sillery, E., Ciccarelli, O., Wheeler-Kingshott, C., Thompson, A., Smith, S., Matthews, P.: Functional-anatomical validation and individual variation of diffusion tractography-based segmentation of the human thalamus. Cereb. Cortex **15**, 31–39 (2005)
18. Jonasson, L., Hagmann, P., Pollo, C., Bresson, X., Wilson, C., Meuli, R., Thiran, J.: A level set method for segmentation of the thalamus and its nuclei in DT-MRI. Signal Process. **87**(2), 309–321 (2007)
19. Jones, D., Horsfield, M., Simmons, A.: Optimal strategies for measuring diffusion in anisotropic systems by magnetic resonance imaging. Magn. Reson. Med. **42**(3), 515–525 (1999)
20. Kaus, M.R., Warfield, S.K., Nabavi, A., Black, P.M., Jolesz, F.A., Kikinis, R.: Automated segmentation of MR images of brain tumors. Radiology **218**(2), 586–591 (2001)
21. Kingsley, P.B.: Introduction to diffusion tensor imaging mathematics: part II. Anisotropy, diffusion-weighting factors, and gradient encoding schemes. Concepts Magn. Reson., Part A, Bridg. Educ. Res. **28A**(2), 123–154 (2006)
22. Kinnard, L.M., Lo, S.C.B., Duckett, E., Makariou, E., Osicka, T., Freedman, M.T., Chouikha, M.F.: Mass segmentation of dense breasts on digitized mammograms: analysis of a probability-based function. In: SPIE Medical Imaging, vol. 5747, pp. 1813–1823 (2005)

23. Klingberg, T., Vaidya, C.J., Gabrieli, J.D.E., Moseley, M.E., Hedehus, M.: Myelination and organization of the frontal white matter in children: a diffusion tensor MRI study. NeuroReport **10**, 2812–2821 (1999)
24. Koay, C.G., Carew, J.D., Alexander, A.L., Basser, P.J., Meyerand, M.E.: Investigation of anomalous estimates of tensor-derived quantities in diffusion tensor imaging. Magn. Reson. Med. **55**(4), 930–936 (2006)
25. Lenglet, C., Rousson, M., Deriche, R.: A statistical framework for DTI segmentation. In: International Symposium on Biomedical Imaging, pp. 794–797 (2006)
26. Maas, L., Mukherjee, P., Carballido-Gamio, J., Veeraraghavan, S., Miller, S., Partridge, S., Henry, R., Barkovich, A., Vigneron, D.: Early laminar organization of the human cerebrum demonstrated with diffusion tensor imaging in extremely premature infants. NeuroImage **22**(3), 1134–1140 (2004)
27. Meyer, F.: The dynamics of minima and contours. In: International Symposium on Mathematical Morphology, pp. 329–336 (1996)
28. Najman, L., Schmitt, M.: Geodesic saliency of watershed contours and hierarchical segmentation. IEEE Trans. Pattern Anal. Mach. Intell. **18**(12), 1163–1173 (1996)
29. Niogi, S., Mukherjee, P., McCandliss, B.: Diffusion tensor imaging segmentation of white matter structures using a reproducible objective quantification scheme (ROQS). NeuroImage **35**, 166–174 (2007)
30. Peeters, T., Rodrigues, P., Vilanova, A., ter Haar Romeny, B.: Analysis of distance/similarity measures for diffusion tensor imaging. In: Farin, G., Hege, H.C., Hoffman, D., Johnson, C.R., Polthier, K., Rumpf, M., Laidlaw, D., Weickert, J. (eds.) Visualization and Processing of Tensor Fields: Advances and Perspectives, Mathematics and Visualization, pp. 113–136. Springer, Berlin (2009)
31. Pennec, X., Fillard, P., Ayache, N.: A Riemannian framework for tensor computing. Int. J. Comput. Vis. **66**(1), 41–66 (2006)
32. Pierpaoli, C., Basser, P.: Toward a quantitative assessment of diffusion anisotropy. Magn. Reson. Med. **36**(6), 893–906 (1996)
33. Rettmann, M., Han, X., Xu, C., Prince, J.: Automated sulcal segmentation using watersheds on the cortical surface. NeuroImage **15**(2), 329–344 (2002)
34. Rittner, L., Lotufo, R.: Diffusion tensor imaging segmentation by watershed transform on tensorial morphological gradient. In: Brazilian Symp. on Computer Graph. and Image Proc, pp. 196–203 (2008)
35. Rittner, L., Lotufo, R.A.: Segmentation of DTI based on tensorial morphological gradient. In: Proceedings of SPIE, vol. 7259, p. 72 (2009). SPIE
36. Rittner, L., Flores, F., Lotufo, R.: New tensorial representation of color images: tensorial morphological gradient applied to color image segmentation. In: Brazilian Symp. on Computer Graph. and Image Proc, pp. 45–52 (2007)
37. Rittner, L., Flores, F., Lotufo, R.: A tensorial framework for color images. Pattern Recognit. Lett. **31**(4), 277–296 (2010)
38. Skare, S., Li, T., Nordell, B., Ingvar, M.: Noise considerations in the determination of diffusion tensor anisotropy. Magn. Reson. Imaging **18**(6), 659–669 (2000)
39. Vachier, C., Meyer, F.: Extinction value: a new measurement of persistence. In: Workshop on Nonlinear Signal and Image Processing, vol. 1, pp. 254–257 (1995)
40. Vincent, L., Soille, P.: Watersheds in digital spaces: an efficient algorithm based on immersion simulations. IEEE Trans. Pattern Anal. Mach. Intell. **13**(6), 583–598 (1991)
41. Wang, Z., Vemuri, B.: DTI segmentation using an information theoretic tensor dissimilarity measure. IEEE Trans. Med. Imaging **24**(10), 1267–1277 (2005)
42. Weldeselassie, Y., Hamarneh, G.: DT-MRI segmentation using graph cuts. In: SPIE Medical Imaging, vol. 6512, pp. 1–9 (2007)
43. Wiegell, M., Tuch, D., Larson, H., Wedeen, V.: Automatic segmentation of thalamic nuclei from diffusion tensor magnetic resonance imaging. NeuroImage **19**, 391–402 (2003)
44. Zhukov, L., Museth, K., Breen, D., Whitaker, R., Barr, A.: Level set modeling and segmentation of DT-MRI brain data. J. Electron. Imaging **12**, 125–133 (2003)
45. Ziyan, U., Tuch, D., Westin, C.: Segmentation of thalamic nuclei from DTI using spectral clustering. In: Medical Image Computing and Computer-Assisted Intervention, pp. 807–814 (2006)

Leticia Rittner obtained a M.Sc. degree in Electrical Engineering from State University of Campinas and a Ph.D. degree in Computer Engineering also from the University of Campinas, with a 6-month internship at the Montreal Neurological Institute, McGill University, Canada. Dr. Rittner is a research associate at the School of Electrical and Computer Engineering, University of Campinas and holds at present a post-doctorate at the School of Medicine, University of Pennsylvania. Her main research interests are image processing and analysis, pattern recognition and medical imaging, with emphasis on diffusion MRI.

Jennifer S.W. Campbell is a research associate at the McConnell Brain Imaging Centre, Montreal Neurological Institute, McGill University. She obtained her B.Sc. (Honours) degree in Mathematics and Physics from Queen's University. She then obtained M.Sc. and Ph.D. degrees in Medical Physics and Biomedical Engineering, respectively, from McGill University. Her research focuses on acquisition and post processing of diffusion magnetic resonance imaging (MRI) data.

Pedro F. Freitas received a M.Sc. degree in Computer Engineering in 2012 from the School of Electrical and Computer Engineering from the University of Campinas, Brazil. He received a B.Sc. degree in Electrical Engineering in 2009 from the same institution. His main interests are in Image Processing and Analysis, Mathematical Morphology and Medical Imaging.

Simone Appenzeller has received the M.D. and Ph.D. degrees from Faculty of Medical Science, State University of Campinas. Appenzeller was a Postdoc at McGill University, Canada and at Stavanger Hospital, Norway. She is an Assistant Professor at the Rheumatology Department, Faculty of Medical Science, State University of Campinas. Dr. Appenzeller research focused on neurologic manifestations and neuroimaging in rheumatic diseases.

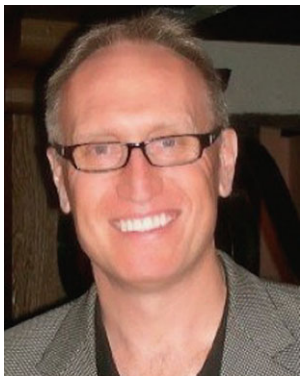

G. Bruce Pike is the Killam Professor of Neurology & Neurosurgery and James McGill Professor of Biomedical Engineering at McGill University. He is also Director of the McConnell Brain Imaging Centre at the Montreal Neurological Institute and is a National Researcher of Quebec. Following an undergraduate degree in Electrical Engineering he obtained his M.Sc. and Ph.D. at McGill University with his research focused on stereotactic radiosurgery and magnetic resonance angiography, respectively. He then conducted postdoctoral studies at Stanford University. Dr. Pike joined the faculty of McGill University in 1994 where he investigates magnetic resonance imaging (MRI) methods and applications for basic and clinical neuroscience research.

Roberto A. Lotufo obtained the Electronic Engineering Diploma from Instituto Tecnologico de Aeronautica, Brazil, in 1978, and the Ph.D. degree from the University of Bristol, U.K., in 1990, in Electrical Engineering. He is a full professor at the School of Electrical and Computer Engineering, University of Campinas (Unicamp), Brazil, were he has worked for since 1981. His principal research interests are in the areas of Image Processing and Analysis, Mathematical Morphology, Pattern Recognition and Medical Imaging. Prof. Lotufo has published over 150 refereed international journal and full conference papers. He is the executive director of Inova Unicamp (www.inova.unicamp.br), the agency for innovation at Unicamp, since 2004. Lotufo was awarded the Innovation Personality in 2008 and the Zeferino Vaz Academic Recognition in 2011.